p53 Regulates Nuclear Architecture to Reduce Carcinogen Sensitivity and Mutagenic Potential

Devin A. King, Dakota E. McCoy, Adrian Perdyan, Jakub Mieczkowski, Thierry Douki, Jennifer A. Dionne, Rafael E. Herrera, Ashby J. Morrison

Corresponding author: ashbym@stanford.edu

The PDF file includes:

Materials and Methods

Cell Culture

IMR-90 (cat. no. I90-83) and WI-38 primary fibroblasts (cat. no. AG06814) were obtained from Coriell Institute. Primary neonatal keratinocytes (cat. no. C0015C) and melanocytes (cat. no. C0025C) were obtained from Thermo Fisher Scientific. All cells were grown in media recommended by the respective vendor. All experiments were performed prior to passage 16.

TP53 CRISPR-Cas9 guide RNA was designed with the E-CRISP design tool (*1*). Guide RNA sequences: 5′- GCTTGTAGATGGCCATGGCG -3′; 3′-CGAACATCTACCGGTACCGC-5′ were cloned into lentiCRISPR plasmid (Addgene, cat. no. 49535) and transfected into HEK293T cells with VSV-g, psPAX2 to produce virus to transduce primary IMR-90 cells. Puromycin resistant cells were pooled. TP53 disruption was confirmed by Western blot using anti-p53 antibody (Cell Signaling, cat. no. 9282) and anti-Emerin antibody (Cell Signaling, cat. no. 5430) as a loading control.

UV Tag-Seq Experimental Methods

Cyclobutane pyrimidine dimers (CPDs) were investigated in this study because CPDs are the most abundant and mutagenic UVB-induced lesion, compared to (6-4) photoproducts and Dewar isomers (*2*).

Cells were grown to confluency for 48 hours, then irradiated with 200 J/m^2 UVB, or 100 J/m^2 UVC, followed by immediate (< 10 seconds) cell lysis and DNA purification with Quick-gDNA MiniPrep (Zymo Research, cat. no. D3007). Lambda spike-in DNA was prepared by irradiating purified bacteriophage lambda DNA (New England Biolabs, cat. no. N3011) with 100 J/m^2 UVC. For each sample, 100ngs of high molecular weight genomic DNA and 5ngs of lambda spike-in were treated with APE1 apurinic/apyrimidinic (AP) endonuclease (New England Biolabs, cat. no. M0282), Bst1 polymerase (New England Biolabs, cat. no. M0328) and Taq ligase (New England Biolabs, cat. no. M0208) to repair possible gaps/nicks and abasic sites in the DNA. After purification using Zymo Genomic DNA Clean & Concentrator (D4011), the DNA was processed to cleave at CPDs using T4 PDG (NEB, M0308). The resulting 3'-α, β-unsaturated aldehyde and 5'-phosphate termini were removed by APE1 and Quick CIP (NEB, M0525) to prepare the DNA ends for subsequent ligation. DNA was again purified with Zymo Genomic DNA Clean & Concentrator (D4011). dsDNA was denatured with alkali (400 mM KOH, 10 mM EDTA, pH 8) for three minutes before neutralization with 800 mM Tris HCl, pH 4.

Barcoded biotinylated adapters were ligated onto the processed 3’-OH single-stranded DNA using 4000 units of high-concentration T4 Ligase (New England Biolabs, cat. no. M0202) and 20% final concentration of PEG 8000 overnight at 16°C. Unligated adapters were removed using PCRClean DX (Aline Biosciences, cat. no. C-1003). Ligations from each library were then inactivated and added to a multiplexed pool. Adapter-ligated DNA was captured on MyOne Streptavidin C1 beads (Invitrogen, cat. no. 65001) according to the manufacturer's instructions. Second strand synthesis by nick extension was performed by first nicking the adaptor with Nt.BspQI (NEB, cat. no. R0644S), then extending with LongAmp Taq Master Mix (NEB, M0287S). Beads were subsequently washed to remove strand synthesis reagents. The distal adapter was inserted in processed DNA fragments using tagmentation with Tn5 transposase at 55°C, followed by extensive washing of beads. DNA fragments were released from the beads by heat denaturation, followed by immediate pelleting to remove beads and transfer of eluant to LoBind tubes (Eppendorf, cat. no. 4043-1021).

After the number of optimal PCR cycles were determined using qPCR libraries, DNA was amplified with Ultra II Q5 Master Mix (NEB, cat. no. M0544S), ODK74_P7umi, and NEBNext Universal PCR Primer for Illumina (NEB, cat. no. E7335S). Library quality was assessed with the Agilent High Sensitivity D1000 TapeStation and Qubit HS dsDNA assays. Final libraries were double-side size-selected with sequential 0.75x and 0.2x PCRClean DX bead additions before sequencing on an Illumina NovaSeq in paired-end, single index 2 x 150 cycle configuration.

UV Tag-Seq Computational Methods

Raw sequencing reads were de-multiplexed and adapter-trimmed using cutadapt. Read quality was assessed with FastQC, and UMI information was recovered using a custom awk script. Reads were aligned to a concatenated lambda-hg19 genome using STAR, quality filtered, and de-duplicated using samtools. Resulting BAM files were split by species to extract spike-in reads from human reads. Human reads overlapping ENCODE blacklisted regions were discarded. BED files were then generated by shifting each read to cover two bases immediately five-prime to the original alignment position. The reverse complement of these two bases was tallied. Final signal tracks were filtered to include only reads corresponding to TT, TC, CT, and CC dinucleotide sequences. A minimum of 80M high-quality uniquely mapped reads with a dipyrimidine end were obtained for each sample.

Lesion counts were tallied across the genome in different windows ranging from 1 Kb to 1 Mb. Scree plots and PCA were used to determine that 50kb sliding windows were appropriate for subsequent analysis. Dispersion estimates, along with negative binomial linear model fitting and Wald statistics, were used to assess the suitability of the data for analysis using DESeq2. Genomic bins with fewer than 100 reads were removed. Count matrices were used as input to the DESeq2 algorithm with default parameters except that size factors were manually overridden with human/lambda spike-in ratios. Top DSRs were defined as genomic windows with FDR-adjusted $\alpha < 0.00001$ and $|\log_2 FC| > 1$.

RNA-Seq

RNA was extracted using Quick-RNA Miniprep Kit (cat. no. R1054). Total RNA was purified using NEBNext rRNA Depletion Kit v2 (cat. no. E7400). Library prep was performed using NEBNext Ultra II Directional RNA Library Prep Kit (cat. no. E7760) and NEBNext Multiplex Oligos for Illumina (Unique Dual Index UMI Adaptors RNA Set 1) (cat. no. E7416) with Lexogen SIRV-Set 3 (Iso Mix E0 / ERCC) (cat. no. 051.01) spike-in. Sequencing was performed on Illumina NovaSeq with a minimum of 170 million mapped reads per sample (2 technical replicates).

RNA-Seq was processed using nf-core/rna-seq pipeline with default parameters and the T2T-CHM13v2.0 reference genome. For analysis of samples produced in this study, UMI deduplication was performed, and spike-in scaling factors were determined using Lexogen SIRVsuite (v0.1.2). DESeq2 was used to determine differential expression (Table S1). Enrichment of KEGG pathways was performed using ShinyGO.

For comparative analysis with other studies that treat IMR-90 (GSE58740, GSE115940, GSE111437) and U2OS (GSE84863) cells with DNA damage (*3–5*), all datasets were processed using the nf-core/rna-seq pipeline with default parameters and the T2T-CHM13v2.0 reference genome. Normalization was performed using Trimmed Mean of M-values (TMM), batch correction using ComBat, and differential expression with limma.

Epigenomic Analysis

Chromatin states and ChIP-Seq signal track files for E017 (IMR-90) were taken from the Roadmap Epigenomics Project (*6*). Lamin B1 ChIP-Seq data was obtained from (GSE49341) (*7*), and re-processed using the ENCODE DCC ChIP-seq pipeline 2 (https://github.com/ENCODE-DCC/chip-seq-pipeline2) for conformity with Roadmap Epigenomics data. Signal tracks were aggregated in 10 kb bins and composite signals were plotted over composite DSRs. In heatmaps, $-\log_{10}$ P-value were scaled by row.

Mass Spectrometry of Cyclobutane-Pyrimidine Dimers (CPDs)

DNA was extracted from frozen UV-irradiated cell pellets by first purifying nuclei followed by lysis. Lysate was treated with RNase and proteinase, then DNA was precipitated with sodium iodide and isopropanol, as previously described (*8*). The lyophilized DNA pellet was hydrolyzed into monomer nucleotides by incubation with endonucleases, exonucleases, and phosphodiesterases, first at pH 5.5 and then at pH 8.0. Injected samples were first assessed for normal bases by a reverse-phase HPLC with a UV detector. Subsequently, fragments from all UV-induced pyrimidine dimeric photoproducts (*9*) were specifically and sensitively analyzed using an electrospray mass spectrometer with triple quadrupole analyzer in "multiple reaction monitoring" mode. DNA was quantified using an external calibration with reference compounds. Pyrimidine dimers were quantified by internal calibration using [M+12]-isotopically labeled TT photoproducts as standards, as previously described (*10*).

p53 ChIP-Seq and XR-Seq Analysis

p53 ChIP-Seq peak datasets for the hg19 genome were obtained from ENCODE for A549 (ENCFF699UTZ, n=6207), HepG2 (ENCFF701DTE, n=7621) and WTC11 (ENCFF403HEQ, n=8037) cell lines (*11*). Overlap of p53 signal within DSRs at specific genomic regions was assessed using the GenomicDistributions R package. Cumulative XR-Seq nucleotide excision repair signal (GSE76391) was calculated from Adar et al, 2016 (*12*).

Melanoma Mutation Analysis

Mutations from 2,922 deep-sequenced tumors from the Pan-cancer Analysis of Whole Genomes project and 100 tumors from the Brazilian project SKCA-BR were retrieved from ICGC (*13*, *14*). Tumor mutation rates were computed in the same 50 kb bins used for DSR analysis. Simple somatic mutations and mutational signatures were extracted using the R MutationalPatterns package. Cosmic Mutational Signatures (v3.4) were previously determined (*15*, *16*).

3D Genome Modeling and Fluorescent Imaging

A three-dimensional volumetric model of the IMR-90 genome in the nucleus was previously generated (*17*) using the Chrom3D modeling technique which incorporates lamin-mapping and Hi-C genome contacts to simulate spatial positioning of chromosomes relative to each other and the nuclear periphery (*18*, *19*).

For fluorescent imaging, cells were grown on coverslips to confluency then fixed for 10 mins at room temperature with 4% fresh formaldehyde. Cells were permeabilized with 0.5% TritonX-100 for 5 minutes on ice then blocked with 2.5% bovine serum albumin (BSA), 10% Normal Goat Serum, 0.1% Tween-20 for 30 minutes at room temperature. Anti-lamin B1 antibody (Abcam cat. no. ab16048) was added to blocking buffer overnight at 4°C. Washed cells were mounted with DAPI and imaged on Leica SP8 with 60x objective.

Fluorescent images were analyzed using CellProfiler (v4.2.5) using default settings for "MeasureObjectSizeShape" and "MeasureObjectDistribution" (*20*). Intensity measurements were excluded (Table S2). A Random Forest algorithm was derived from the tidymodels package to create a machine-learning pipeline that classifies cell types based on image-derived features. Principal Component Analysis (PCA) used features that explain 75% of the variance between TP53KO and wild-type cells.

Transmission Electron Microscopy (TEM)

Cells were pelleted and re-suspended in 10% gelatin in 0.1M sodium cacodylate buffer (pH 7.4) at 37°C for 5 minutes. After re-pelleting and removing excess gelatin, cells were fixed in 1% osmium tetroxide (EMS cat. no. 19100) for 2 hours at 4°C. The fixed cells were washed with cold ultrafiltered water and stained overnight with 1% uranyl acetate at 4°C. The samples were dehydrated through a graded ethanol series (30%, 50%, 70%, 95%) for 20 minutes each at 4°C, followed by two washes in 100% ethanol at room temperature. Subsequent processing involved propylene oxide (PO) and infiltration with Embed-812 resin (EMS cat. no. 14120), using graded resin mixtures (1:2, 1:1, 2:1) for 2 hours each. After overnight rotation in 2:1 resin at room temperature, samples were embedded in fresh Embed-812 resin and polymerized at 65°C overnight. Approximately 80nm sections were put on formvar/Carbon coated 100 mesh Cu grids, stained for 30 seconds in 3.5% Uranyl Acetate in 50% Acetone followed by staining in 0.2% lead citrate for 3 minutes. Sections were imaged in JEOL JEM-1400 120kV and photos were taken using a Gatan Orius 4k X 4k digital camera.

Nuclear periphery density was measured by creating a mask outline of the nuclear periphery in Fiji (*21*) from each of seven EM images for both TP53KO and wild-type cells. For each image, ten randomly selected regions spanning the mask were measured, from the inner to the outer region, and line lengths were quantified and scaled according to image magnification.

Light Transmission Simulations

Finite-difference time-domain simulations were performed on TEM images cropped to the nuclear boundary (*22*). ANSYS Lumerical Software binarized the image and assigned black pixels to represent heterochromatin and gray pixels to represent euchromatin. Refractive indices and extinction coefficients were previously determined (*23*) and assigned to euchromatin, n=1.385, k=0.0001; heterochromatin n=1.415, k=0.01; and background cytoplasm, n=1.365. Simulations of UVB light transmission into the nuclear interior were measured using a plane wave light source centered at 306 nm, the UVB wavelength used in the experimental manipulations.

Computational Methods

Computational programs used in this study are listed in Table 3.

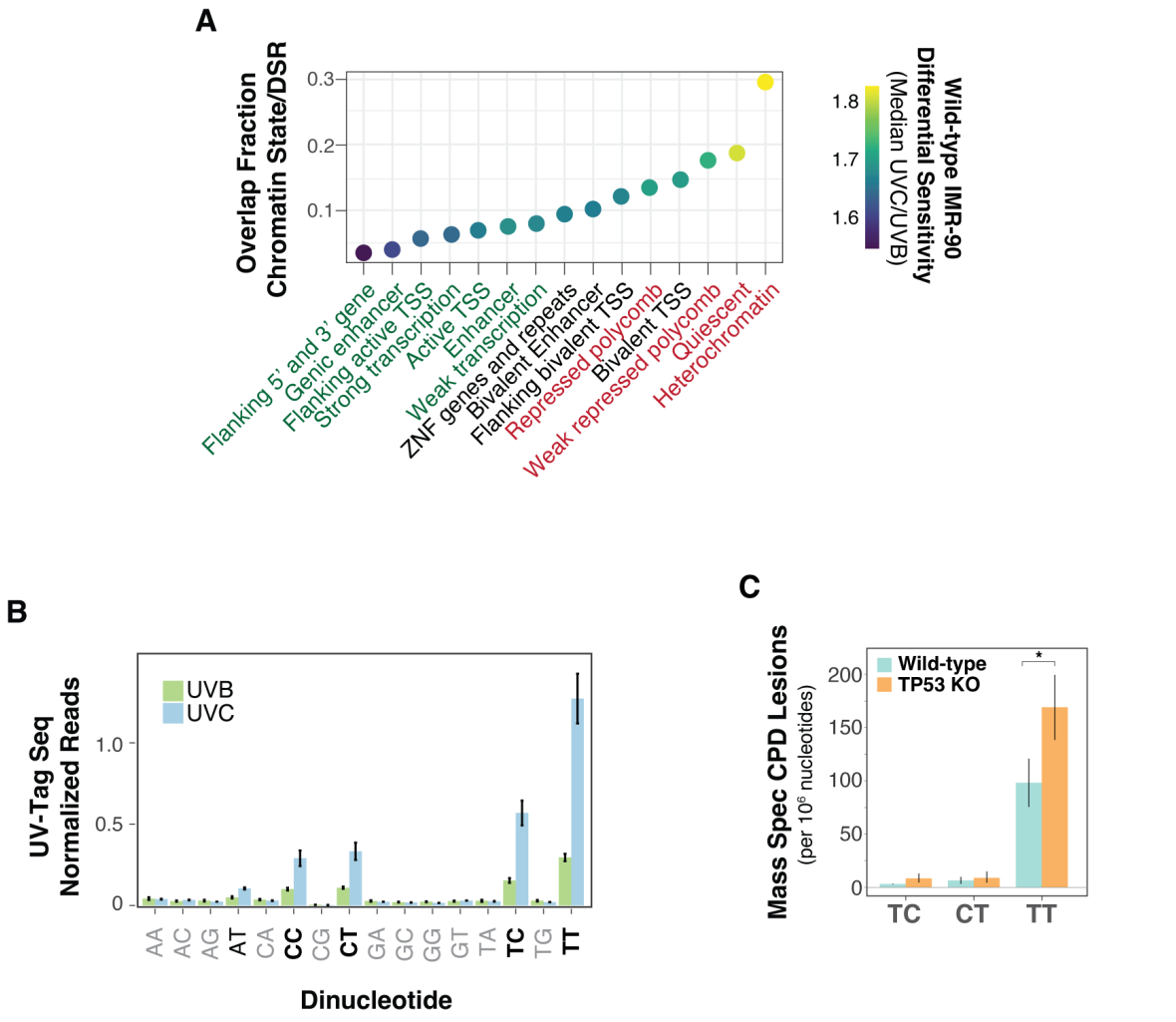

fig. S1. Confirmation of UV-Tag Method. (A) Enrichment (fraction overlap) of different chromatin states, defined by the Roadmap Epigenomic Consortium, in UVC vs UVB Differentially Susceptible Regions (DSRs). The color of the dot indicates the median UV Tag-Seq signal within that chromatin state. The color of the chromatin state name indicates euchromatin (green), heterochromatin (red), or bivalent/mixed (black). **(B)** Counts of UV Tag-Seq reads that align to different dipyrimidine sequences. Lambda spike-in was used to calculate Spike-in normalized Reads Per Million mapped reads in the negative Control (SRPMC). Error bars represent the standard error of the mean. **(C)** Quantitative mass spectrometry counts of different cyclobutane pyrimidine dimers (CPDs) from UVB-irradiated cells. * indicates p-value >0.05 from Welch's t-test.

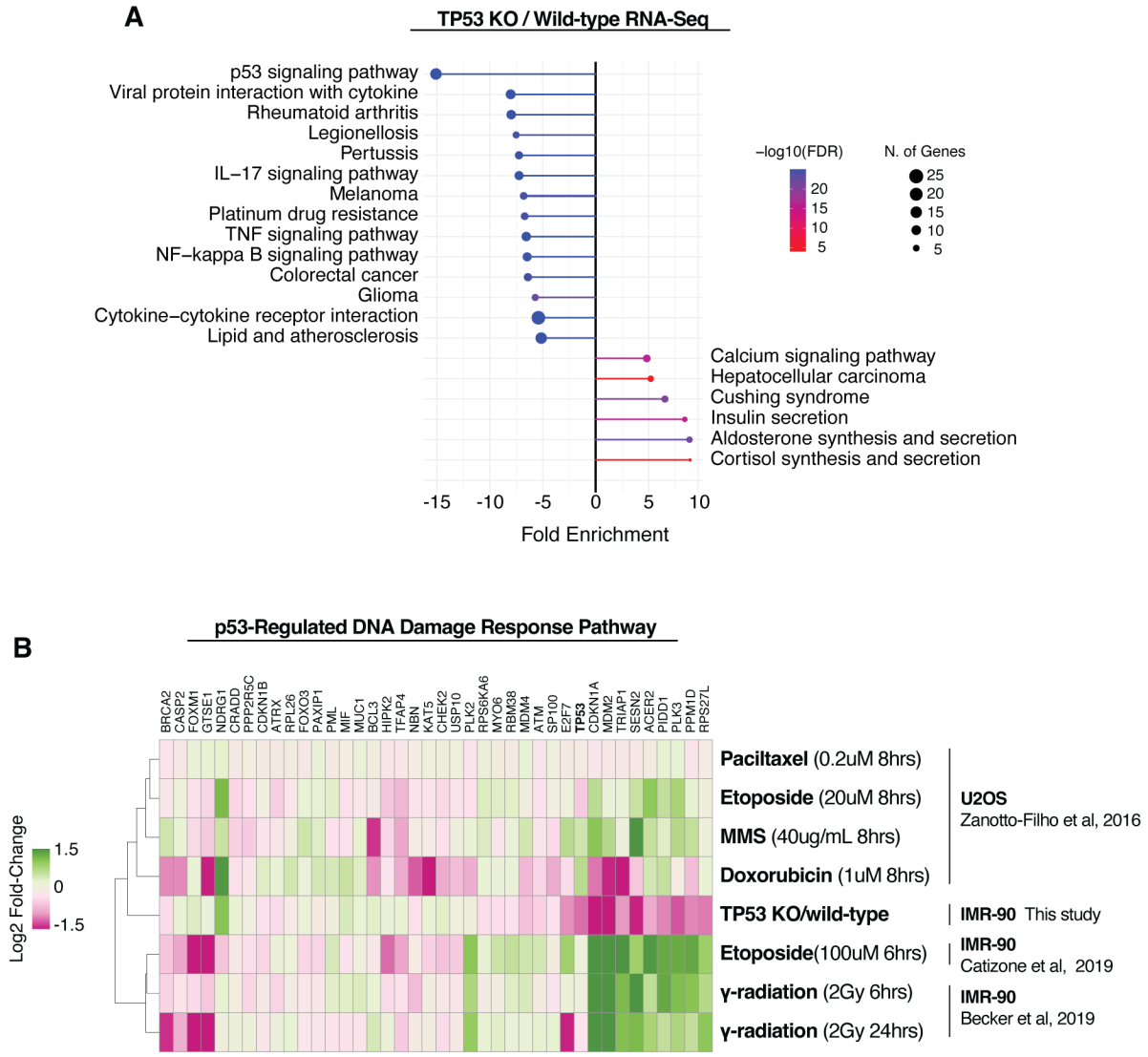

fig. S2. TP53 KO RNA-Seq and comparisons with cells treated with DNA damage. (A) KEGG Pathway enrichment of RNA-seq differential expression from TP53 KO vs wild-type cells. **(B)** Heatmap of RNA-Seq Log_2 Fold-Changes for genes in the GO:0030330 "DNA damage response, signal transduction by p53 class mediator" pathway for the indicated cells exposed to DNA damage compared to unexposed/wild-type. TP53 KO vs wild-type IMR-90 cells were treated with 200 UVB J/m^2.

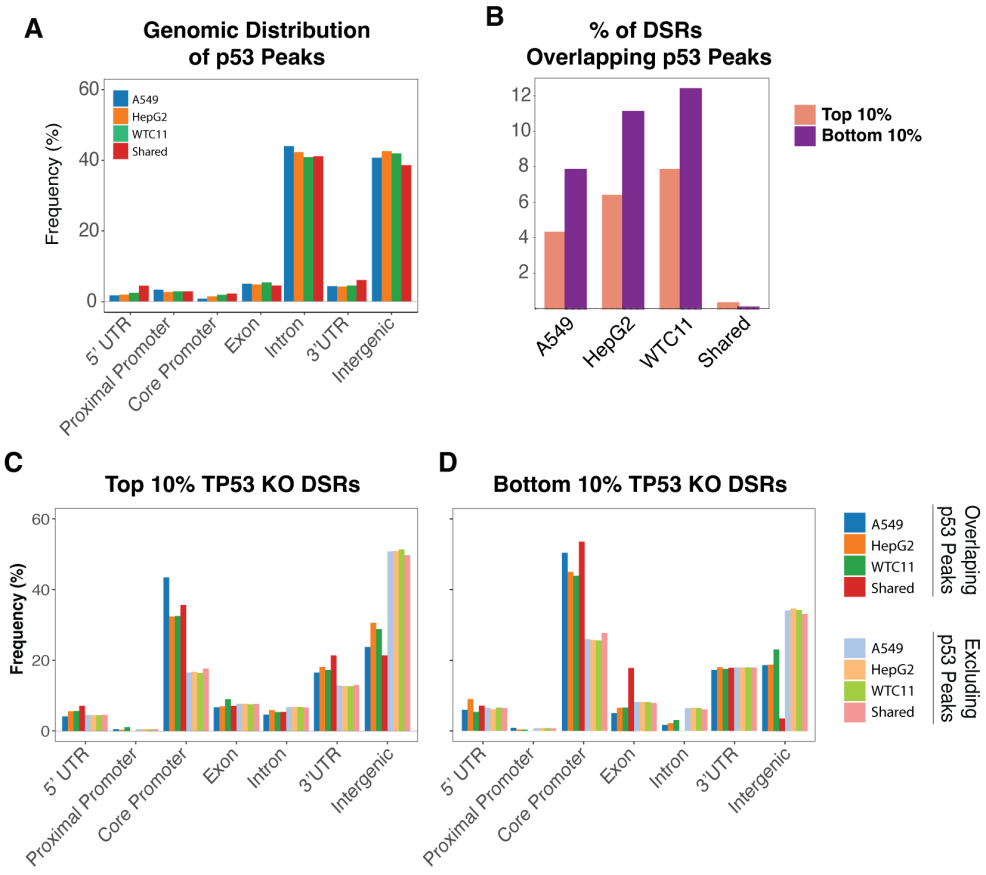

fig S3. Most TP53 binding sites are not located within TP53 KO Differentially Susceptible Regions (DSRs). (A) Genomic distribution of TP53 ChIP-seq peaks from indicated cell lines (ENCODE). N=6207 for A549; N=7621 for HepG2; N= 8037 for WTC11. Shared are the peaks common between all cell lines, N=311. **(B)** The percentage of top and bottom 10% DSRs that overlap TP53 ChIP-seq peaks. **(C)** Genomic distribution of DSRs that overlap and exclude p53 peaks in the top 10% DSRs, **(D)** and bottom 10% DSRs.

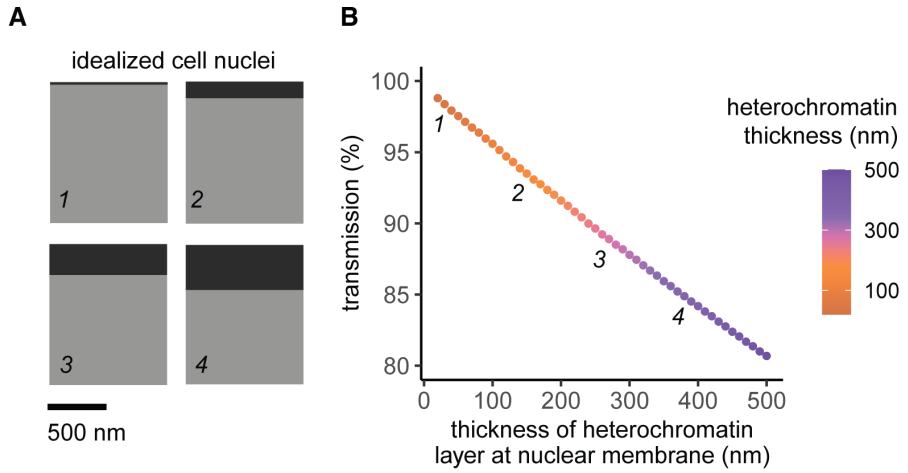

fig. S4. Validation of light transmission simulations. Finite-difference time-domain used on idealized cross-sections of the cell nucleus, where the amount of heterochromatin at the nuclear membrane varied from 10nm to 500nm. To ensure consistency, the relative refractive indices were varied, and consistent results were found.

TABLE 3. Computational References

Program	version	citation
R	4.3.1	The R Project for Statistical Computing. https://www.R-project.org/
ggplot2	3.5.1	Hadley Wickham. ggplot2: Elegant Graphics for Data Analysis, 2016.
BRGenomics	1.12.0	Kwak H, Fuda NJ, Core LJ, Lis JT. Precise maps of RNA polymerase reveal how promoters direct initiation and pausing. Science. 2013 Feb 22;339(6122):950-3. doi: 10.1126/science.1229386. PMID: 23430654; PMCID: PMC3974810.
cutadapt	4.9	Martin M. Cutadapt removes adapter sequences from high-throughput sequencing reads. EMBnet journal. DOI: https://doi.org/10.14806/ej.17.1.200
FASTQC	0.12.0	Andrews, S. FastQC: A Quality Control Tool for High Throughput Sequence Data. https://www.bioinformatics.babraham.ac.uk/projects/fastqc/
samtools	1.2	Li H, Handsaker B, Wysoker A, Fennell T, Ruan J, Homer N, Marth G, Abecasis G, Durbin R; 1000 Genome Project Data Processing Subgroup. The Sequence Alignment/Map format and SAMtools. Bioinformatics. 2009 Aug 15;25(16):2078-9. doi: 10.1093/bioinformatics/btp352. Epub 2009 Jun 8.
STAR	2.7.11b	Dobin A, Davis CA, Schlesinger F, Drenkow J, Zaleski C, Jha S, Batut P, Chaisson M, Gingeras TR. STAR: ultrafast universal RNA-seq aligner. Bioinformatics. 2013 Jan 1;29(1):15-21. doi: 10.1093/bioinformatics/bts635. Epub 2012 Oct 25. PMID: 23104886; PMCID: PMC3530905.
nf-core		Ewels PA, Peltzer A, Fillinger S, Patel H, Alneberg J, Wilm A, Garcia MU, Di Tommaso P, Nahnsen S. The nf-core framework for community-curated bioinformatics pipelines. Nat Biotechnol. 2020 Mar;38(3):276-278. doi: 10.1038/s41587-020-0439-x. PMID: 32055031.
nf-core/rnaseq	3.13.2	https://github.com/nf-core/rnaseq. DOI: 10.5281/zenodo.1400710
DESeq2	1.40.2	Love MI, Huber W, Anders S. Moderated estimation of fold change and dispersion for RNA-seq data with DESeq2. Genome Biol. 2014;15(12):550. doi: 10.1186/s13059-014-0550-8. PMID: 25516281; PMCID: PMC4302049.
circlize	0.4.16	Gu Z, Gu L, Eils R, Schlesner M, Brors B. circlize Implements and enhances circular visualization in R. Bioinformatics. 2014 Oct;30(19):2811-2. doi: 10.1093/bioinformatics/btu393. Epub 2014 Jun 14. PMID: 24930139.
EnhancedVolcano	1.18.0	Blighe, K, S Rana, and M Lewis. 2018. "EnhancedVolcano: Publication-ready volcano plots with enhanced colouring and labeling." https://github.com/kevinblighe/EnhancedVolcano.
GenomicRanges	1.54.1	Lawrence M, Huber W, Pagès H, Aboyoun P, Carlson M, Gentleman R, Morgan MT, Carey VJ. Software for computing and annotating genomic ranges. PLoS Comput Biol. 2013;9(8):e1003118. doi: 10.1371/journal.pcbi.1003118. Epub 2013 Aug 8. PMID: 23950696; PMCID: PMC3738458.
ComBat		Johnson WE, Li C, Rabinovic A. Adjusting batch effects in microarray expression data using empirical Bayes methods. Biostatistics. 2007 Jan;8(1):118-27. doi: 10.1093/biostatistics/kxj037. Epub 2006 Apr 21. PMID: 16632515.
edgeR	3.42.4	Robinson MD, McCarthy DJ, Smyth GK. edgeR: a Bioconductor package for differential expression analysis of digital gene expression data. Bioinformatics. 2010 Jan 1;26(1):139-40. doi: 10.1093/bioinformatics/btp616. Epub 2009 Nov 11. PMID: 19910308; PMCID: PMC2796818.
limma	3.56.2	Ritchie ME, Phipson B, Wu D, Hu Y, Law CW, Shi W, Smyth GK. limma powers differential expression analyses for RNA-sequencing and microarray studies. Nucleic Acids Res. 2015 Apr 20;43(7):e47. doi: 10.1093/nar/gkv007. Epub 2015 Jan 20. PMID: 25605792; PMCID: PMC4402510.
TMM:trimmed mean of M-values		Robinson MD, Oshlack A. A scaling normalization method for differential expression analysis of RNA-seq data. Genome Biol. 2010;11(3):R25. doi: 10.1186/gb-2010-11-3-r25. Epub 2010 Mar 2. PMID: 20196867; PMCID: PMC2864565.
ShinyGO	0.80	Ge SX, Jung D, Yao R. ShinyGO: a graphical gene-set enrichment tool for animals and plants. Bioinformatics. 2020 Apr 15;36(8):2628-2629. doi: 10.1093/bioinformatics/btz931. PMID: 31882993; PMCID: PMC7178415.
KEGG		Kanehisa M, Furumichi M, Sato Y, Ishiguro-Watanabe M, Tanabe M. KEGG: integrating viruses and cellular organisms. Nucleic Acids Res. 2021 Jan 8;49(D1):D545-D551. doi: 10.1093/nar/gkaa970. PMID: 33125081; PMCID: PMC7779016.
pheatmap	1.0.12	Kolde, Raivo. Pretty heatmaps. https://CRAN.R-project.org/package=pheatmap
GenomicDistributions	1.11.1	Kupkova K, Mosquera JV, Smith JP, Stolarczyk M, Danehy TL, Lawson JT, Xue B, Stubbs JT 4th, LeRoy N, Sheffield NC. GenomicDistributions: fast analysis of genomic intervals with Bioconductor. BMC Genomics. 2022 Apr 12;23(1):299. doi: 10.1186/s12864-022-08467-y. PMID: 35413804; PMCID: PMC9003978.
MutationalPatterns	3.14.0	Blokzijl F, Janssen R, van Boxtel R, Cuppen E. MutationalPatterns: comprehensive genome-wide analysis of mutational processes. Genome Med. 2018 Apr 25;10(1):33. doi: 10.1186/s13073-018-0539-0. PMID: 29695279; PMCID: PMC5922316.
tidymodels	1.2.0	Kuhn M, Wickham H (2020). Tidymodels: a collection of packages for modeling and machine learning using tidyverse principles.. https://www.tidymodels.org.
randomForest	4.7-1.1	Wright, M. N., & Ziegler, A. (2017). randomForest: Breiman and Cutler's Random Forests for Classification and Regression. https://cran.r-project.org/web/packages/randomForest/index.html
caret	6.0-94	Kuhn, M. (2008). Building Predictive Models in R Using the caret Package. *Journal of Statistical Software* , *28* (5), 1–26.

1. F. Heigwer, G. Kerr, M. Boutros, E-CRISP: fast CRISPR target site identification. *Nat Methods* **11**, 122–123 (2014).

2. Y. H. You, D. H. Lee, J. H. Yoon, S. Nakajima, A. Yasui, G. P. Pfeifer, Cyclobutane pyrimidine dimers are responsible for the vast majority of mutations induced by UVB irradiation in mammalian cells. *J Biol Chem* **276**, 44688–44694 (2001).

3. A. Zanotto-Filho, V. P. Masamsetti, E. Loranc, S. S. Tonapi, A. Gorthi, X. Bernard, R. M. Gonçalves, J. C. F. Moreira, Y. Chen, A. J. R. Bishop, Alkylating Agent-Induced NRF2 Blocks Endoplasmic Reticulum Stress-Mediated Apoptosis via Control of Glutathione Pools and Protein Thiol Homeostasis. *Mol Cancer Ther* **15**, 3000–3014 (2016).

4. A. N. Catizone, C. R. Good, K. A. Alexander, S. L. Berger, M. A. Sammons, Comparison of genotoxic versus nongenotoxic stabilization of p53 provides insight into parallel stress-responsive transcriptional networks. *Cell Cycle* **18**, 809–823 (2019).

5. B. V. Becker, L. Kaatsch, R. Obermair, G. Schrock, M. Port, R. Ullmann, X-ray irradiation induces subtle changes in the genome-wide distribution of DNA hydroxymethylation with opposing trends in genic and intergenic regions. *Epigenetics* **14**, 81–93 (2019).

6. Roadmap Epigenomics Consortium, A. Kundaje, W. Meuleman, J. Ernst, M. Bilenky, A. Yen, A. Heravi-Moussavi, P. Kheradpour, Z. Zhang, J. Wang, M. J. Ziller, V. Amin, J. W. Whitaker, M. D. Schultz, L. D. Ward, A. Sarkar, G. Quon, R. S. Sandstrom, M. L. Eaton, Y.-C. Wu, A. R. Pfenning, X. Wang, M. Claussnitzer, Y. Liu, C. Coarfa, R. A. Harris, N. Shoresh, C. B. Epstein, E. Gjoneska, D. Leung, W. Xie, R. D. Hawkins, R. Lister, C. Hong, P. Gascard, A. J. Mungall, R. Moore, E. Chuah, A. Tam, T. K. Canfield, R. S. Hansen, R. Kaul, P. J. Sabo, M. S. Bansal, A. Carles, J. R. Dixon, K.-H. Farh, S. Feizi, R. Karlic, A.-R. Kim, A. Kulkarni, D. Li, R. Lowdon, G. Elliott, T. R. Mercer, S. J. Neph, V. Onuchic, P. Polak, N. Rajagopal, P. Ray, R. C. Sallari, K. T. Siebenthall, N. A. Sinnott-Armstrong, M. Stevens, R. E. Thurman, J. Wu, B. Zhang, X. Zhou, A. E. Beaudet, L. A. Boyer, P. L. De Jager, P. J. Farnham, S. J. Fisher, D. Haussler, S. J. M. Jones, W. Li, M. A. Marra, M. T. McManus, S. Sunyaev, J. A. Thomson, T. D. Tlsty, L.-H. Tsai, W. Wang, R. A. Waterland, M. Q. Zhang, L. H. Chadwick, B. E. Bernstein, J. F. Costello, J. R. Ecker, M. Hirst, A. Meissner, A. Milosavljevic, B. Ren, J. A. Stamatoyannopoulos, T. Wang, M. Kellis, Integrative analysis of 111 reference human epigenomes. *Nature* **518**, 317–330 (2015).

7. M. Sadaie, R. Salama, T. Carroll, K. Tomimatsu, T. Chandra, A. R. J. Young, M. Narita, P. A. Pérez-Mancera, D. C. Bennett, H. Chong, H. Kimura, M. Narita, Redistribution of the Lamin B1 genomic binding profile affects rearrangement of heterochromatic domains and SAHF formation during senescence. *Genes Dev* **27**, 1800–1808 (2013).

8. J.-L. Ravanat, T. Douki, P. Duez, E. Gremaud, K. Herbert, T. Hofer, L. Lasserre, C. Saint-Pierre, A. Favier, J. Cadet, Cellular background level of 8-oxo-7,8-dihydro-2'-deoxyguanosine: an isotope based method to evaluate artefactual oxidation of DNA during its extraction and subsequent work-up. *Carcinogenesis* **23**, 1911–1918 (2002).

9. T. Douki, The variety of UV-induced pyrimidine dimeric photoproducts in DNA as shown by chromatographic quantification methods. *Photochem Photobiol Sci* **12**, 1286–1302 (2013).

10. N. Reynaud, L. Belz, D. Béal, D. Bacqueville, H. Duplan, C. Géniès, E. Questel, G. Josse, T. Douki, DNA photoproducts released by repair in biological fluids as biomarkers of the genotoxicity of UV radiation. *Anal Bioanal Chem* **414**, 7705–7720 (2022).

11. An Integrated Encyclopedia of DNA Elements in the Human Genome. *Nature* **489**, 57–74 (2012).

12. S. Adar, J. Hu, J. D. Lieb, A. Sancar, Genome-wide kinetics of DNA excision repair in relation to chromatin state and mutagenesis. *Proceedings of the National Academy of Sciences* **113**, E2124–E2133 (2016).

13. International network of cancer genome projects. *Nature* **464**, 993–998 (2010).

14. A. L. S. A. Vicente, A. Novoloaca, V. Cahais, Z. Awada, C. Cuenin, N. Spitz, A. L. Carvalho, A. F. Evangelista, C. S. Crovador, R. M. Reis, Z. Herceg, V. de Lima Vazquez, A. Ghantous, Cutaneous and acral melanoma cross-OMICs reveals prognostic cancer drivers associated with pathobiology and ultraviolet exposure. *Nat Commun* **13**, 4115 (2022).

15. Z. Sondka, N. B. Dhir, D. Carvalho-Silva, S. Jupe, null Madhumita, K. McLaren, M. Starkey, S. Ward, J. Wilding, M. Ahmed, J. Argasinska, D. Beare, M. S. Chawla, S. Duke, I. Fasanella, A. G. Neogi, S. Haller, B. Hetenyi, L. Hodges, A. Holmes, R. Lyne, T. Maurel, S. Nair, H. Pedro, A. Sangrador-Vegas, H. Schuilenburg, Z. Sheard, S. Y. Yong, J. Teague, COSMIC: a curated database of somatic variants and clinical data for cancer. *Nucleic Acids Res* **52**, D1210–D1217 (2024).

16. L. B. Alexandrov, J. Kim, N. J. Haradhvala, M. N. Huang, A. W. Tian Ng, Y. Wu, A. Boot, K. R. Covington, D. A. Gordenin, E. N. Bergstrom, S. M. A. Islam, N. Lopez-Bigas, L. J. Klimczak, J. R. McPherson, S. Morganella, R. Sabarinathan, D. A. Wheeler, V. Mustonen, PCAWG Mutational Signatures Working Group, G. Getz, S. G. Rozen, M. R. Stratton, PCAWG Consortium, The repertoire of mutational signatures in human cancer. *Nature* **578**, 94–101 (2020).

17. B. S. Perez, K. M. Wong, E. K. Schwartz, R. E. Herrera, D. A. King, P. E. García-Nieto, A. J. Morrison, Genome-wide profiles of UV lesion susceptibility, repair, and mutagenic potential in melanoma. *Mutat Res* **823**, 111758 (2021).

18. J. Paulsen, M. Sekelja, A. R. Oldenburg, A. Barateau, N. Briand, E. Delbarre, A. Shah, A. L. Sørensen, C. Vigouroux, B. Buendia, P. Collas, Chrom3D: three-dimensional genome modeling from Hi-C and nuclear lamin-genome contacts. *Genome Biol* **18**, 21 (2017).

19. J. Paulsen, T. M. Liyakat Ali, P. Collas, Computational 3D genome modeling using Chrom3D. *Nat Protoc* **13**, 1137–1152 (2018).

20. D. R. Stirling, M. J. Swain-Bowden, A. M. Lucas, A. E. Carpenter, B. A. Cimini, A. Goodman, CellProfiler 4: improvements in speed, utility and usability. *BMC Bioinformatics* **22**, 433 (2021).

21. J. Schindelin, I. Arganda-Carreras, E. Frise, V. Kaynig, M. Longair, T. Pietzsch, S. Preibisch, C. Rueden, S. Saalfeld, B. Schmid, J.-Y. Tinevez, D. J. White, V. Hartenstein, K. Eliceiri, P. Tomancak, A. Cardona, Fiji: an open-source platform for biological-image analysis. *Nat Methods* **9**, 676–682 (2012).

22. K. Yee, Numerical solution of initial boundary value problems involving maxwell's equations in isotropic media. *IEEE Transactions on Antennas and Propagation* **14**, 302–307 (1966).

23. I. Solovei, M. Kreysing, C. Lanctôt, S. Kösem, L. Peichl, T. Cremer, J. Guck, B. Joffe, Nuclear Architecture of Rod Photoreceptor Cells Adapts to Vision in Mammalian Evolution. *Cell* **137**, 356–368 (2009).